Chapter 3

System – Ag_3

3.1 Introduction

Small silver clusters represent an interesting and challenging subject for ultrafast molecular dynamics. These systems have been extensively studied before, yielding a wealth of information on their spectroscopic properties [76–78], structure and energetics [79–81]. Recent studies have indicated, that silver miniclusters play a key role in the process of the formation of photographic images [82, 83], a fact, which highlights the importance of understanding their fundamental photochemical properties. This work is concerned with the investigation of the dynamics of silver trimers in the gas phase, and was triggered by the pioneering experiment in the group of Wöste on NeNePo spectroscopy of Ag_3 [84, 85].

The acronym NeNePo stands for **Ne**gative-to-**Ne**utral-to-**Po**sitive ion spectroscopy, which has its roots in pump-probe spectroscopy proposed by Zewail [3, 86–88], and photodetachment spectroscopy of Neumark [89, 90]. This approach is also called charge reversal spectroscopy [91]. The technique can be summarized as follows. One starts from an ensemble of anions, jet-cooled and mass-selected. This ensemble is then irradiated by two subsequent ultrashort (typically of femtosecond duration

) laser pulses, the time delay between which can be varied. The first pulse detaches an electron from the anion, and neutral molecules or clusters are formed. Since the equilibrium geometries of anions and neutrals are typically different, the neutrals are formed in a nonequilibrium state, and undergo fast geometric relaxation on femtosecond or picosecond time scale. The process of relaxation is monitored by the second laser pulse, which detaches another electron, and the resulting cations are collected, and their yield measured. This approach allows, firstly, to form neutral molecules or clusters with high degree of vibrational excitation, and, secondly, to follow the process of its redistribution on the time scale of molecular motions.

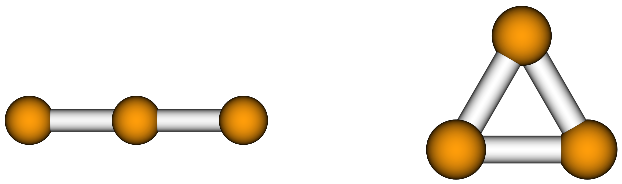

(a) Ag_3^- (b) Ag_3^0,Ag_3^+

Figure 3.1: Two characteristic equilibrium configurations of Ag_3 ions

In the specific case of silver trimers, it has been known from previous *ab initio* calculations [79, 80], that the Ag_3 anions have linear equilibrium geometry in the ground electronic state, and the neutrals and cations have triangular equilibrium configuration (isosceles for Ag_3^0 due to Jahn-Teller effect, and equilateral for Ag_3^+) (see Figure 3.1). Therefore, one should expect fast geometrical relaxation in this system after the photoionization of anions, which was indeed observed in the experiments [84, 91, 92]. For a survey of the experimental results, see [93].

The relevant physical processes occuring in the NeNePo process can be summarized as follows. Upon photodetachment by the first pulse (pump pulse), the neutral species are prepared in a highly nonequilibrium state, and relax to their equilibrium triangular geometry. The geometrical relaxation from the linear Ag_3 to the triangular nuclear configuration is investigated by a delayed ionizing probe pulse using two-photon ionisation. The schematic of the process is shown in Figure 3.2. The

transitions induced by laser pulses are treated as having vertical Franck-Condon type character, and the probe pulses of different wavelengths probe the wavepacket dynamics at three characteristic regions of the potential energy surface (PES): the 6.5 eV pulse monitors the dynamics in the vicinity of the linear configuration, the 5.8 eV probes the region of equilibrium triangular geometry, and the 6.1 eV pulse is chosen as an intermediate point. It has to be noted, that the probing step is

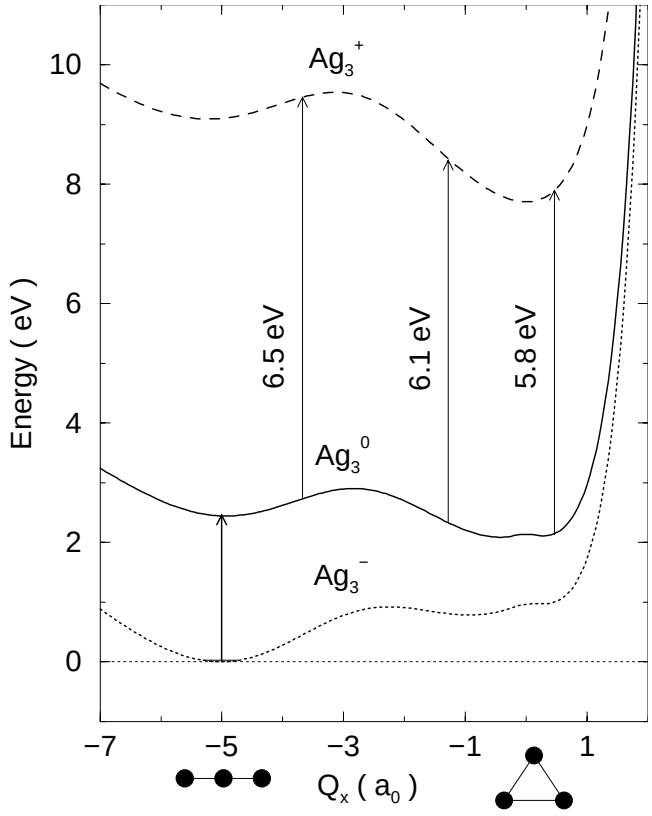

Figure 3.2: Schematic representation of NeNePo experiment in Ag_3. Shown are the one-dimensional cuts through the 3-D *ab initio* PES's [79, 80] of different Ag_3 ions along the bending coordinate Q_x.

achieved via the two-photon ionization, either resonant or nonresonant. A rigorous description of the multiphoton excitation is not possible within the present model, and the two-photon probe is approximated by a one-photon one, with the photon energy double that in the two-photon process. That is why one-photon-kind tran-

sitions are shown in Figure 3.2. The cations produced by the second ionization are collected, and their yield is analyzed as a function of the delay time between the pump and probe pulses, and the probe pulse wavelength. Later experiments in the group of Wöste [94] also investigated the role of the vibrational temperature of the initial anionic ensemble.

Taking into account the physics of the process, one should expect that the yield of Ag_3 cations at a given probe two-photon energy, e.g. 5.8 eV, should be close to zero at zero delay time between the pulses, since this energy is not sufficient to ionize the neutrals from their linear configuration, but should rise at later times, when the representative wave packet approaches the region of the PES, from which the ionization is possible. At even longer delay times, the cation yield should slowly decrease, as the IVR sets in. Such behaviour of the signals was indeed observed in the experiments, first in the group of Wöste, then in the group of Lineberger, where an extension of the NeNePo pump-probe technique using two-color excitation and sensitive ion and electron detection was applied to the study of $Ag_3^-/Ag_3/Ag_3^+$ system. [91].

First theoretical confirmation of the experimental results was provided by Jeschke et al. [95, 96]. In their calculations, microscopic electronic theory within a tight-binding model was combined with molecular dynamics simulations, yielding the information on the time-dependent changes of the ionization potential (IP) of Ag_3. It was found, that with the pump photon energies corresponding to those of experiment, the trimer can only be ionized after a certain delay time, in their case ≈ 750 fs. With further increase of the delay time, the signal slightly decreases, and reaches saturation, which was interpreted as a statistical effect induced by temperature.

Subsequent theoretical studies of the multi-state nuclear dynamics based on classical trajectories on the ground electronic adiabatic PES of Ag_3^-, Ag_3 and Ag_3^+ (obtained from accurate *ab initio* quantum chemistry calculations) and the simulations of the pump-probe femtosecond signals utilizing the Wigner representation of the vibrational density matrix by Hartmann et al. [97, 98] elucidated the rich dynamics of this system. In these studies it has been shown that the dynamics of the Ag_3 cluster initiated from the linear transition state involves, in addition to the

configurational relaxation towards the triangular geometry, sequential intracluster vibrational relaxation (IVR) processes, which can dominate the intracluster dynamics. These processes involve intracluster collisions, the onset of IVR, resonant and dissipative IVR and vibrational equilibration, whose time scales were determined. Furthermore, their dependence on the initial cluster temperature was discussed. The calculated NeNePo-ZEKE signal and the total, integrated over the photoelectron energy , NeNePo signal allowed to show how geometrical change, completion of IVR and vibrational coherence effects can be identified in the signals.

The first full-dimensional quantum dynamical simulations of the dynamics of silver trimers in the process of NeNePo were obtained in this thesis, see Ref. [99]. In these simulations the same adiabatic ground state PES's as in [97,98] have been used, which enables a close comparison between the semiclassical and quantum mechanical treatments. The characteristic features of the process of geometric relaxation in neutral silver trimers have been observed, including the intracluster collision, onset and evolution of IVR, vibrational equilibration. The influence of the temperature of the initial anionic ensemble has also been studied. These topics, and the comparison of quantum mechanical and semiclassical approaches for treatment of molecular dynamics shall be the main focus of this chapter.

3.2 Model and Techniques

In this investigation, the vibrational dynamics of neutral Ag trimers, as induced by NeNePo spectroscopy [84,91], is simulated by the time evolution of a representative three dimensional wave packet. These three dimensions correspond to the normal modes of a trimer in the vicinity of the equilibrium D_{3h} equilateral triangular geometry. The modes considered are the symmetric stretch mode Q_s, the bending mode Q_x, and the asymmetric stretch mode Q_y. The potential energy surfaces for the Ag_3^-, Ag_3^0 and Ag_3^+ of Ref. [97, 98] are represented in terms of these normal modes.

Since a nonrotating planar triatomic molecule has three vibrational degrees of freedom, a set of three nuclear coordinates should be sufficient for the description of

vibrational motion of silver trimer. However, the question of suitability of the three normal vibrational modes of an equilateral triangular molecule for the description of the system arises, since the normal modes are always defined with respect to a certain equilibrium reference configuration, and in the case of the silver trimer we have to deal with large amplitude motion, from the linear to triangular configuration. Nevertheless, it can be shown that the coordinates chosen are quite adequate for the dynamical simulations.

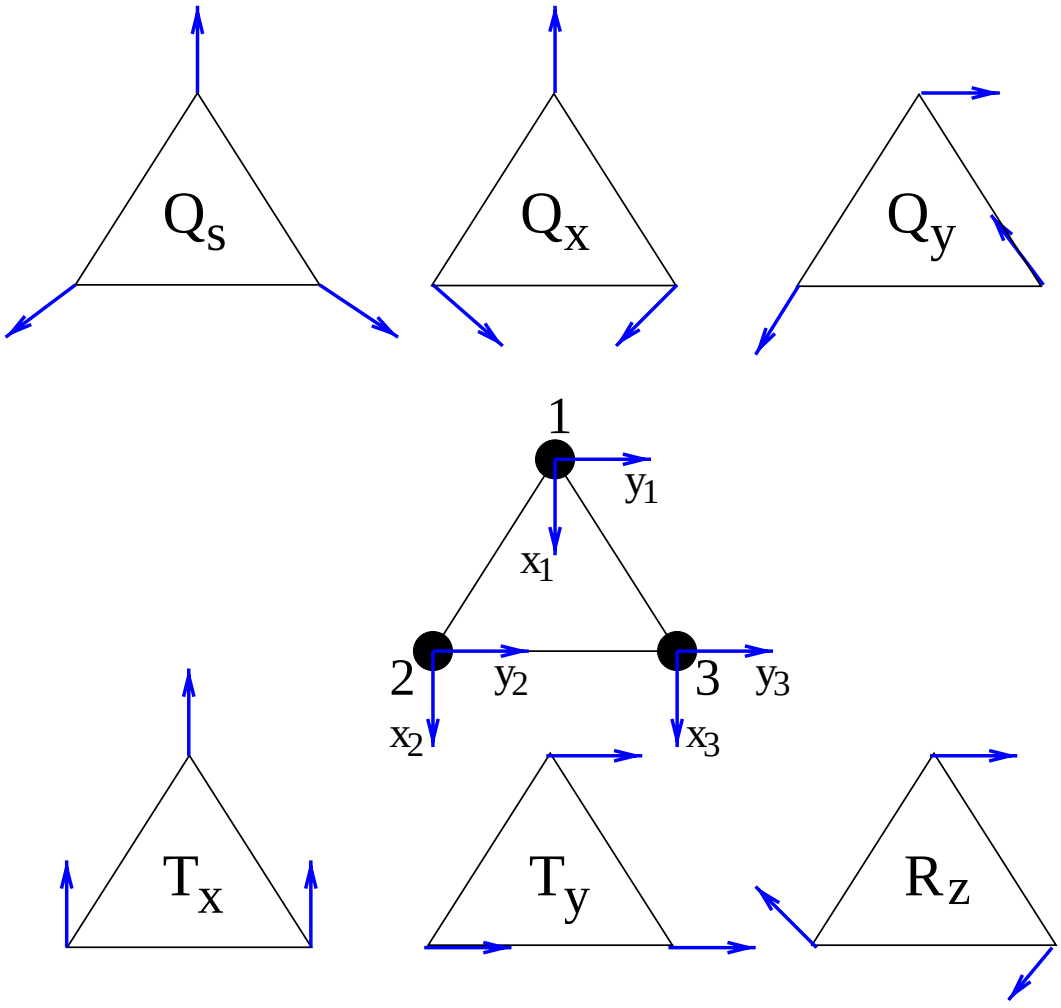

Figure 3.3: Vibrational normal coordinates of a triatomic molecule in the vicinity of the D_{3h} equilibrium geometry.

The normal coordinates of a triatomic molecule, defined with respect to the equilateral triangular equilibrium configuration, are defined as follows [42, 100]:

$$\begin{pmatrix} T_x \\ T_y \\ R_z \\ Q_s \\ Q_x \\ Q_y \end{pmatrix} = \frac{1}{\sqrt{3}} \begin{pmatrix} -1 & 0 & -1 & 0 & -1 & 0 \\ 0 & 1 & 0 & 1 & 0 & 1 \\ 0 & 1 & -\frac{\sqrt{3}}{2} & -\frac{1}{2} & \frac{\sqrt{3}}{2} & -\frac{1}{2} \\ -1 & 0 & \frac{1}{2} & -\frac{\sqrt{3}}{2} & \frac{1}{2} & \frac{\sqrt{3}}{2} \\ -1 & 0 & \frac{1}{2} & \frac{\sqrt{3}}{2} & \frac{1}{2} & -\frac{\sqrt{3}}{2} \\ 0 & 1 & \frac{\sqrt{3}}{2} & -\frac{1}{2} & -\frac{\sqrt{3}}{2} & -\frac{1}{2} \end{pmatrix} \begin{pmatrix} x_1 \\ y_1 \\ x_2 \\ y_2 \\ x_3 \\ y_3 \end{pmatrix}, \tag{3.1}$$

where $x_i, y_i; i = 1, 2, 3$ are the Cartesian displacements from the equilibrium configuration, T_x, T_y are the translational modes, R_z is the uniform rotation about the z axis, Q_s, Q_x, Q_y are the symmetric stretch, bending, and asymmetric stretch modes, respectively. The normal coordinates are schematically represented in Figure 3.3.

Applying the general procedure for derivation of quantum mechanical Hamilton operator (cf. Appendix C), we obtain the following expression for the kinetic energy part of the Hamiltonian:

$$\hat{\mathrm{T}} = \frac{1}{2m} \left(\frac{\partial^2}{\partial Q_s^2} + \frac{\partial^2}{\partial Q_x^2} + \frac{\partial^2}{\partial Q_y^2} + \frac{\partial^2}{\partial T_x^2} + \frac{\partial^2}{\partial T_y^2} + \frac{\partial^2}{\partial R_z^2} \right). \tag{3.2}$$

Here $m = m(\mathrm{Ag})$ is the mass of one silver atom. The Cartesian-like separation of terms in the Hamiltonian and the absence of kinetic coupling between the normal modes is one of the major advantages of the normal coordinate description of dynamics. When the amplitudes of the vibrations in the vicinity of the equilibrium configuration are small, the translational and rotational motions can be separated out of the Schrödinger equation and disregarded. In the case of silver trimers, however, the changes in R_z influence the internuclear distances, and the rotational mode has to be taken into account, increasing the dimensionality of the problem to four.

Such increase in the number of degrees of freedom is not necessarily harmful, since it greatly simplifies the vibrational Hamiltonian. For example, the three-dimensional Hamilton operator (4.15) in Chapter 4 contains complicated kinetic

couplings, the treatment of which can become prohibitive with the increase in the grid sizes for propagation, whereas the simple form of the equation (3.2) can make the computation feasible, even in four dimensions.

In the calculations of the dynamics of silver trimers, however, the R_z mode has been neglected. This is justified, since the theoretical estimates of the relative magnitude of the kinetic energy in the R_z mode have indicated that at any given time it contains less than 5% of the total kinetic energy (typically less than 1%, except for the regions in the close vicinity of linear configuration). The procedure used to prove these facts can be outlined as follows. The kinetic energy operator (3.2) was subjected to several constraints, which included the conservation of the total angular momentum, fixing the position of the molecular center of mass to the origin, neglecting the translational motions. In the vicinity of the linear molecular configuration, where the influence of the R_z mode is the greatest, we know from the semiclassical simulations [97], that the asymmetric stretch Q_y mode is inactive at the beginning of the propagation. Reference [97] also gives the amounts of kinetic energy located in each of the normal modes at any given time. Taking into account all the above, one can calculate the relative difference of the kinetic energy T_{R_z} of the R_z mode (i.e. the expectation value of the $\partial^2/\partial R_z^2$)to the kinetic energy T_{others} contained in other modes (Q_x and Q_s, since we treat the Q_y mode as inactive at initial stages of the dynamics). This ratio, given by the equation

$$R = \frac{|T_{R_z} - T_{\text{others}}|}{T_{\text{others}}}, \tag{3.3}$$

is shown in the Figure 3.4. As we can see from this figure, in the regions close to the linear molecular geometry ($Q_s = -Q_x \approx 5a_0$), the R_z mode never gets more than 5% of the energy. In the region of triangular geometry the assumption that the asymmetric stretch mode is inactive loses its validity, resulting in greater deviation. However, in the vicinity of the triangular equilibrium geometry R_z is representing a pure rotation and can be safely discarded. The fact that the rotational R_z mode contains negligible amounts of kinetic energy was also independently confirmed in the semiclassical simulations of Hartmann and coworkers [101].

The dynamics of the system was first investigated by solving the coupled time-

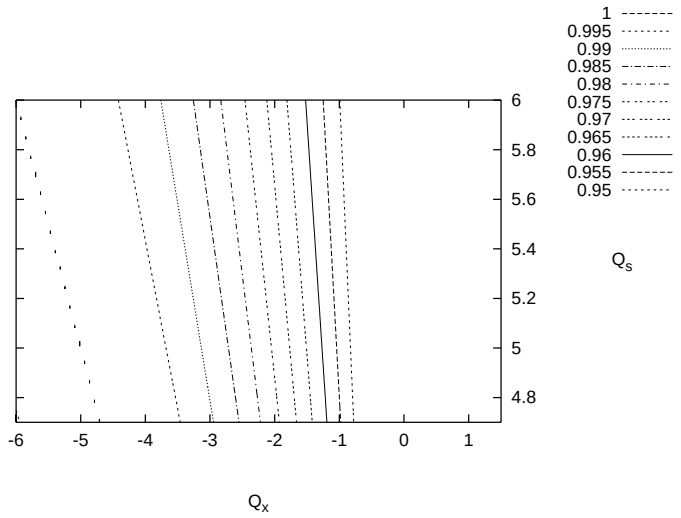

Figure 3.4: The relative difference between the amount of the kinetic energy in the R_z mode and the others at the initial stages of dynamics.

dependent Schrödinger equations

$$i\hbar\frac{\partial}{\partial t}\begin{pmatrix}\Psi_{\mathrm{A}}\\ \Psi_{\mathrm{N}}\\ \Psi_{\mathrm{C}}\end{pmatrix} = \begin{pmatrix}\hat{\mathrm{T}}+\hat{\mathrm{V}}_{\mathrm{A}} & \hat{\mathrm{W}}_{\mathrm{AN}} & 0\\ \hat{\mathrm{W}}_{\mathrm{AN}} & \hat{\mathrm{T}}+\hat{\mathrm{V}}_{\mathrm{N}} & \hat{\mathrm{W}}_{\mathrm{NC}}\\ 0 & \hat{\mathrm{W}}_{\mathrm{NC}} & \hat{\mathrm{T}}+\hat{\mathrm{V}}_{\mathrm{C}}\end{pmatrix}\begin{pmatrix}\Psi_{\mathrm{A}}\\ \Psi_{\mathrm{N}}\\ \Psi_{\mathrm{C}}\end{pmatrix} \tag{3.4}$$

where $\Psi_i = \Psi_i(Q_x, Q_y, Q_s; t), i = \mathrm{A}, \mathrm{N}, \mathrm{C}$ are the three-dimensional time-dependent wave functions moving on the PES's of the anion, neutral and cationic silver trimer respectively in their electronic ground states; $\hat{\mathrm{T}}$ is the kinetic energy operator given by the equation (3.2); $\hat{\mathrm{V}}_i = \hat{\mathrm{V}}_i(Q_x, Q_y, Q_s)$ is the potential energy; $\hat{\mathrm{W}}_j = -\mu_j\mathcal{E}(t), j = \mathrm{AN}, \mathrm{NC}$ is the electromagnetic field interaction term in electric dipole approximation, where μ_j is the transition dipole moment for the anion-neutral and neutral-cation transitions respectively. The transition dipole moment for both the pump and the probe transitions was assumed to be independent of the nuclear coordinates, corresponding to the so-called Condon approximation. For the pump

excitation this approach is reasonable, since the initial and promoted wave functions are localized in the small region of the PES. For the probe excitation this approach might be less suitable, because of the large amplitude motions involved. However, the *ab initio* data on the transition dipole moment was not available, making the Condon approximation imperative.

The electric field of the laser is defined as follows:

$$\mathcal{E}(t) = \sum_{k=\mathrm{pu,pr}} \mathcal{E}_k \mathrm{e}^{-\frac{(t-t_k)^2}{\tau_k^2}} \cos(\omega_k t). \tag{3.5}$$

In the expression (3.5) we label two subsequent nonoverlapping pulses with gaussian envelopes of widhts τ_{pu}, τ_{pr} centered at times t_k, carrier frequencies ω_{pu},ω_{pr}, and field strengths $\mathcal{E}_{\mathrm{pu}}, \mathcal{E}_{\mathrm{pr}}$ by pump (pu) and probe (pr), respectively. The time delay between the pump and probe laser pulses is $t_d = t_{\mathrm{pr}} - t_{\mathrm{pu}}$. In the following applications, the field strengths $\mathcal{E}_{\mathrm{pu}}, \mathcal{E}_{\mathrm{pr}}$ were chosen small enough so that intrapulse pump-dump processes were negligible. The relative NeNePo signal is then independent of $\mathcal{E}_{\mathrm{pu}}$ and $\mathcal{E}_{\mathrm{pr}}$. The coupled equations (3.4) correspond to simulations of NeNePo-ZEKE spectra, i.e. for zero kinetic energy of the photodetached electron. In the more general case of NeNePo spectra with arbitrary electron energies, the electronic continuum should be taken into account, see e.g. the one-dimensional model simulation in Ref. [102]. Application of such an approach for the 3-D model of Ag_3 proved to be prohibitively expensive for the available computer resources. The equations (3.4) were propagated in time using the split operator method, the time step Δt being equal to 0.24 fs, and the diagonalization of the Hamilton matrix at each time step was avoided by using a modified integral equation approach, as in [58, 103].

The procedure outlined above proved to be computationally demanding, so that only two-dimensional or a few three-dimensional calculations could be carried out, for exemplary choices of the laser parameters. For routine simulations of the NeNePo-ZEKE spectra, including systematic variations of the delay times, approximations had to be introduced. The optical excitation was treated using the quantum analog of the expression for the NeNePo-ZEKE signals from Ref. [97], to carry out a close comparison of quantum and semiclassical treatments. The pump

pulse of zero duration ($\tau_{\mathrm{pu}} = 0$) promotes the initial wavepacket from the anionic surface to that of a neutral unchanged, and the NeNePo signal scales with the density of the wave function accumulated in the Franck-Condon window of the probe pulse as follows:

$$S(t_d) \sim \sum_G \mathrm{e}^{-\frac{\tau_{\mathrm{pr}}^2}{\hbar^2}\{E_{\mathrm{pr}} - V_{\mathrm{NC}}(Q_x,Q_y,Q_s)\}^2} |\Psi_{\mathrm{N}}(Q_x, Q_y, Q_s; t_d)|^2, \tag{3.6}$$

where $S(t_d)$ is the NeNePo-ZEKE signal after (delay) time t_d, $E_{\mathrm{pr}} = 2\hbar\omega_{\mathrm{pr}}$ is the two-photon probe energy, V_{NC} is the energy gap between the cationic and neutral surface, and G is a predetermined set of grid points, over which the summation is

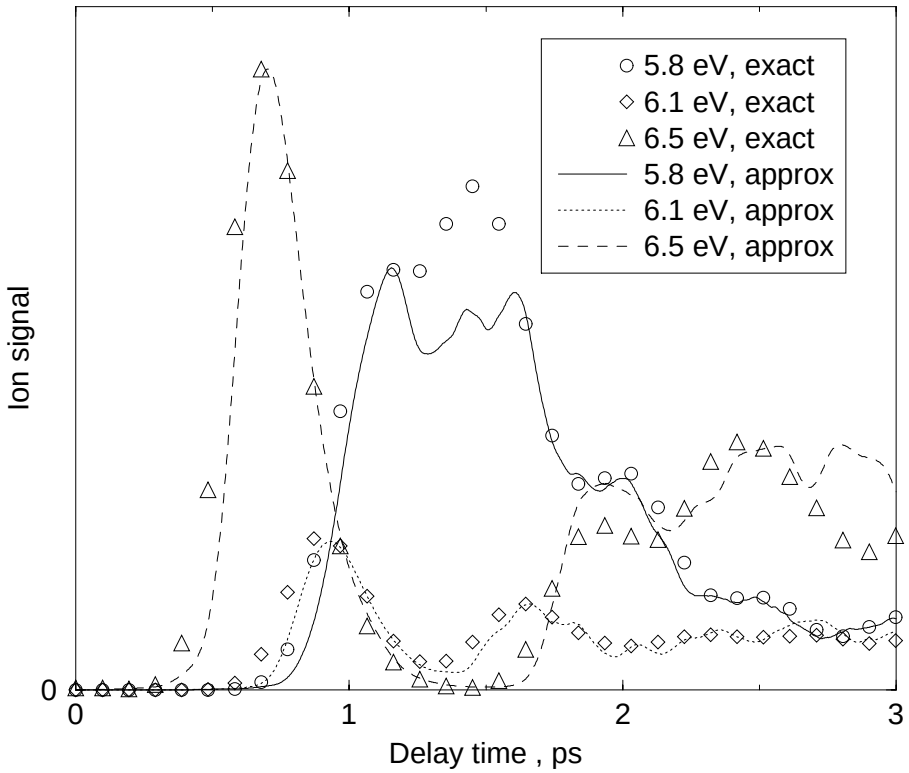

Figure 3.5: Comparison between the NeNePo signals, calculated for different wavelengths of the probe pulse with the exact (equation (3.4)) and approximate (equation (3.6)) methods for a 2-D model, considering the asymmetric stretch (Q_y) mode inactive.

performed. The preliminary two-dimensional simulations have shown that variations

Table 3.1: Grid parameters for the propagation

Coordinate	Min (a_0)	Max (a_0)	Number of points
Q_s	2.5	6.5	256
Q_x	-7.0	1.5	256
Q_y	-1.3	1.3	128

of the widths of the pump pulse in the range 0-100 fs did not affect the resulting signal significantly, due to the slow motion of the heavy silver atoms after the preparation of the neutral cluster.

Using expression (3.6) to calculate the NeNePo-ZEKE spectra, the computational effort is significantly reduced, since it allows us to propagate the wave function only on the PES of neutral Ag_3 instead of three coupled surfaces of (3.4). The approach was tested in two dimensions, by comparing the signals obtained from solving the system of equations (3.4) with the ones calculated with the two-dimensional analog of formula (3.6). The agreement between the two signals was very satisfactory (see Figure 3.5).

In the first, exemplary model simulation, the first excited vibrational eigenstate of Ag_3^-, with energy of 31 cm^{-1} (corresponding to 57 K in units of kT), was chosen as an initial condition, in order to approximate the lowest temperature of a canonical ensemble of trajectories from Ref. [97], i.e. 50 K. The vibrational eigenfunctions of the anion were computed using the direct relaxation method of Tal-Ezer and Kosloff [74].

The parameters of the three-dimensional spatial grid used for the propagation are summarized in Table 3.1. As seen from this table, the wave function has to be represented on a rather dense, albeit wide grid, in order to account for the large amplitude vibrational motion from the linear to the near equilateral triangle configuration. Also, the heavy mass of the silver atom (107.9 a.m.u.) means com-

paratively long time scales of nuclear wavepacket evolution, and a fine, dense grid for the corresponding representation of $\tilde{\psi}$ in the momentum space. The grid size ($256 \times 256 \times 128 = 8388608$ points) and the long propagation times required propagation programs adapted to a massively parallel supercomputer. For the discussion of the details of algorithm parallelization, see Appendix A

3.3 Quantum dynamical propagation

The time evolution of the three-dimensional wave packet on the Ag_3^0 surface is presented in the Figure 3.6 by projecting the total wave function on the Q_x and Q_s coordinates.

The symmetry properties of the wave function represented in normal coordinates allow for slight reduction of the size of the quantum dynamical propagation problem. For example, the potential and the wave functions have a symmetry plane $Q_x + Q_s = 0$. Therefore, the propagation of vibrational eigenstate which have a node at the point $Q_x + Q_s = 0, Q_y = 0$ (the first vibrational excited state, for example) can be sped up considerably. It is not sufficient to propagate the lobes lying in one half-plane, since in this case the pronounced spreading of the wave packet breaks the symmetry. On the other hand, when the symmetric parts of the wave packet (two lobes in the case of the first excited vibrational state) are sufficiently separated, one of them may be damped by an absorbing boundary, whereas the other is used for calculating the observable quantities. Such an approach has been used in the simulation of the evolution of the first vibrational excited state.

It should be noted, that such an approach has several drawbacks. First, it gives incorrect results for the wave functions which have a maximum of density at the point $Q_x + Q_s = 0, Q_y = 0$, like the ground vibrational state. Second, the increase in speed gained that way is not very substantial. In subsequent calculations of the vibrational temperature dependence of the NeNePo-ZEKE signals this approach has been abandoned.

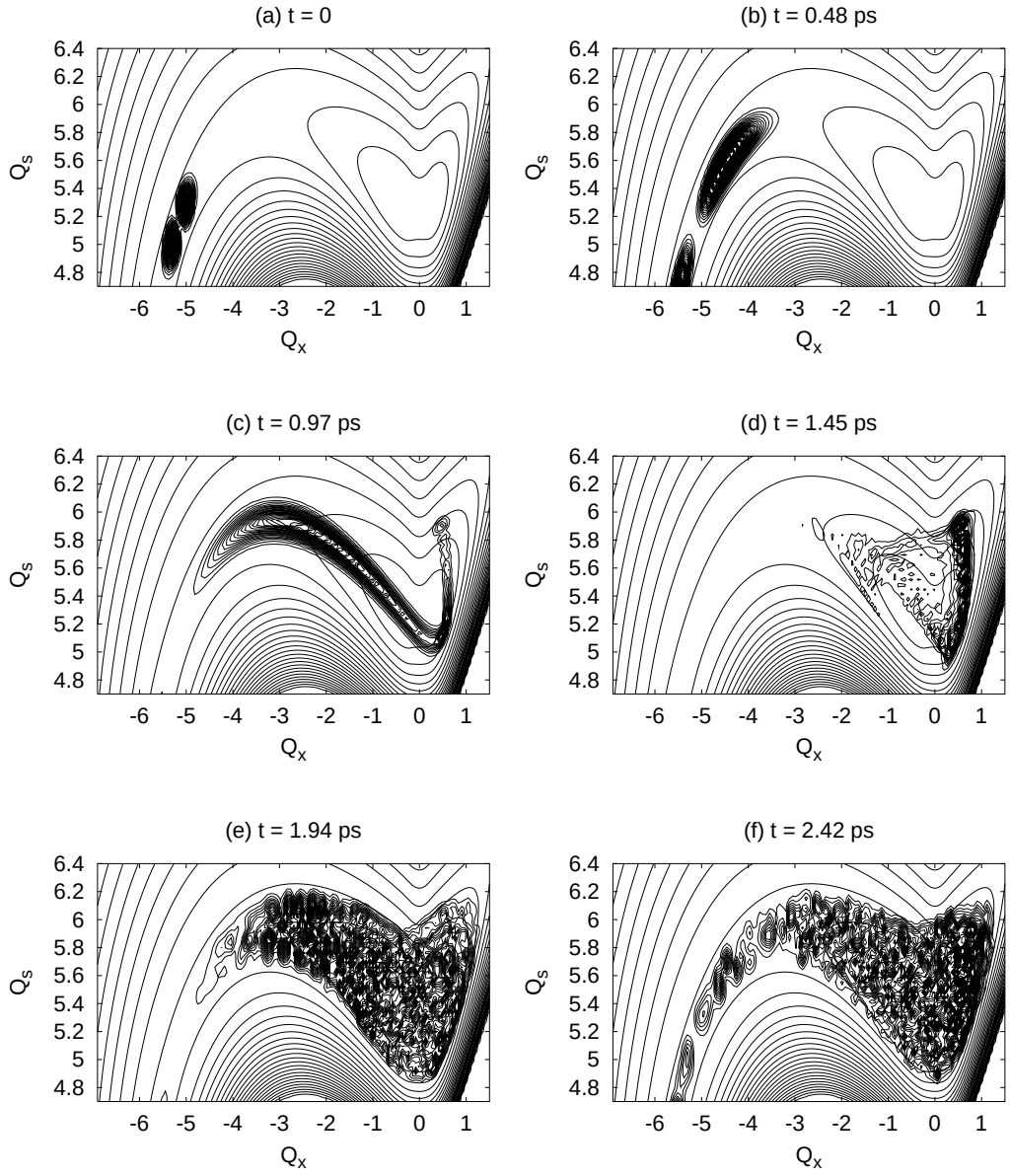

Figure 3.6: Snapshots of the evolution of the wave packet on the Ag_3^0 surface (in normal coordinates). The contour values of the potential energy start at -0.925 E_h, and are incremented by 0.005 E_h. The density of the wave function is represented by 40 equidistant contours from the zero to the maximum density, rescaled for each snapshot.

First, we observe the coherent motion of the wave packet towards the region of equilibrium triangular geometry (Fig. 3.6a and b). This motion corresponds to the bending of the linear trimer, simultaneously accompanied by stretching and subsequent contraction. The asymmetric stretch mode does not play a significant role at this stage. A feature to note is the pronounced spreading behaviour of the wave packet, in spite of some intuitive expectations that a heavy molecule such as a silver trimer should behave "almost classically", that is, the wave packet should remain more localized during the propagation.

At the delay time of ca. 0.8 picoseconds the leading portion of the wavepacket arrives at the region of the equilibrium triangular geometry, where it collides with a rather steep wall of the potential (Figure 3.6c). This corresponds to the event which was discovered by means of classical trajectories in Ref. [97], and called "intracluster collision". The bend cannot proceed any further, and the energy flows into the symmetric stretch mode, where a multi-nodal pattern of the wave function is formed due to interferences of parts of the wave packet, which correspond to subsequent symmetric stretches and compressions, in close analogy to the classical trajectories in Ref. [97] (Fig. 3.6d).

After the intracluster collision, the remaining portion of the wavepacket arrives at the region of equilibrium triangular geometry, causing interference with the preceding partial wave and, therefore, creating complex nodal patterns. In addition, the energy starts to flow also into the asymmetric stretch mode, and we witness the onset of the dissipative intramolecular vibrational redistribution (cf. figures 3.6d and 3.6e).

As the IVR proceeds (Figure 3.6e and f), the wave function gradually fills all available configuration space, and the kinetic energy of the wave packet distributes equally among the three normal modes. The latter phenomenon was first found in the classical simulations of Ref. [97]. The dynamics of the kinetic energy redistribution is shown in Figure 3.7, where different curves show the value of the kinetic energy in the respective normal modes of vibration.

One sees that initially the bending motion is excited, followed by the symmetric

stretching. The asymmetric stretch mode plays a minor role before the intracluster collision, and afterwards acts as an energy sink. From Figure 3.7 we clearly see, that after the time of approximately 2.2 ps the vibrational equilibration is achieved, that is, all modes contain an equal amount of the kinetic energy, marking the completion of IVR.

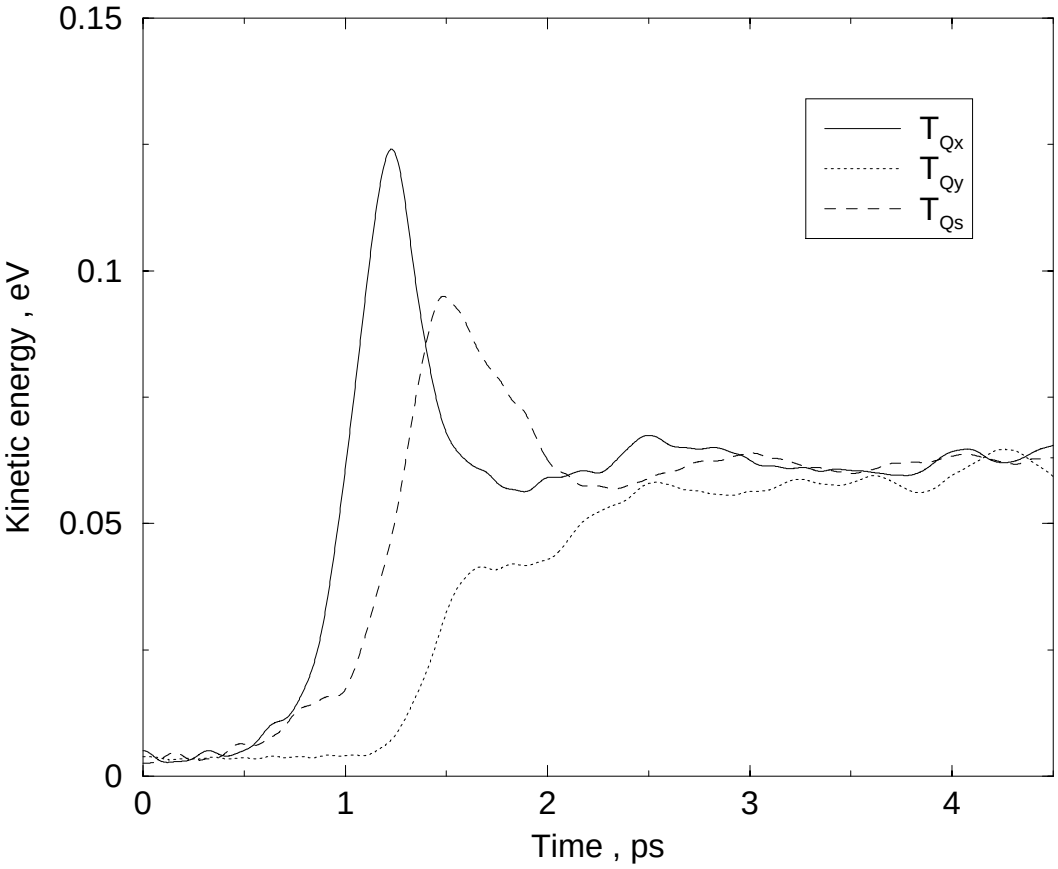

Figure 3.7: The decomposition of the kinetic energy of the evolving wave packet in the normal modes.

Figure 3.6f also shows that a small portion of the wavepacket flows back to the original configuration of the linear trimer – this fractional revival can also be seen in corresponding classical trajectories. The rather weak appearance of this recurrence in Ag_3, in contrast with the observation of fairly coherent revivals in other systems, in particular diatomic molecules [104–108], is a consequence of the dissipative IVR

induced by the intracluster collision.

To gain a better understanding of the dynamics of the Ag_3 cluster, it is also helpful to look at the wave function projected on the Cartesian coordinates. These results are shown in the Figure 3.8. The box in the upper left corner of the snapshots contains the three-dimensional wave function represented as a contour plot in the normal coordinates used for the propagation. In the center of Figs. 3.8a, 3.8b, 3.8c we see the projection of the nuclear wave function on the Cartesian plane. Figure 3.8a represents the initial state, Figure 3.8c shows the wave function at the beginning of the intracluster collision, and Figure 3.8b is chosen as a middle point. One clearly sees the motion from the linear to triangular configuration, and also the pronounced spreading of the wave packets. Thus one sees, that in ultrafast processes the conventional stick-and-ball perception of a molecule has limited applicability.

The quantum dynamical simulation presented here thus complements the earlier semiclassical MD simulations [97], and allows us to establish the correspondence between quantal and classical descriptions of the same system. For comparison, in Figure 3.9a an exemplary snapshot of the wave function at the time t = 1.2 ps is presented together with the corresponding ensemble of classical trajectories of 1.2 ps duration (Figure 3.9b).

We can see that the essential features attributed to the intracluster collision are present in both simulations. There are differences in the behavior of the classical trajectories and the quantal wave packet, for example, the former rebound at a different region of the potential energy surface, but these differences on the microscopic level do not influence the observables dramatically. A feature which is observed only in the quantum simulations is the very complex interference pattern of the three-dimensional wave functions, which originate from the superposition of a large number of eigenstates forming the initial wavepacket, which then evolve with phases due to slightly different energies. The resulting complex nodal pattern (Figures 3.6e, 3.6f) corresponds to classical trajectories with apparently chaotic behaviour.

The resulting quantum mechanical and semiclassical NeNePo-ZEKE spectra for three different frequencies of the probe laser pulse of 100 fs duration are compared

(a)

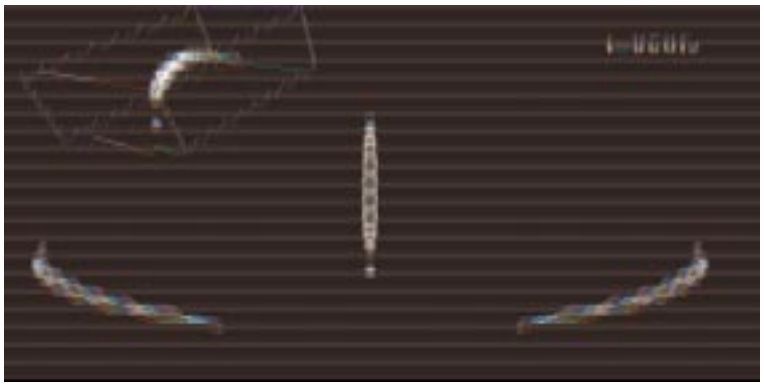

(b)

(c)

Figure 3.8: Evolution of the nuclear wave packets of Ag_3 projected on the Cartesian coordinates (width of the figure - 11 a_0, height - 8 a_0) together with the 3-D probability density contour plots in normal coordinates (The height, width and depth dimensions of the wire box correspond to Q_s,Q_y and Q_x coordinates respectively. The values of the maxima and minima of axes are given in Table 3.1).

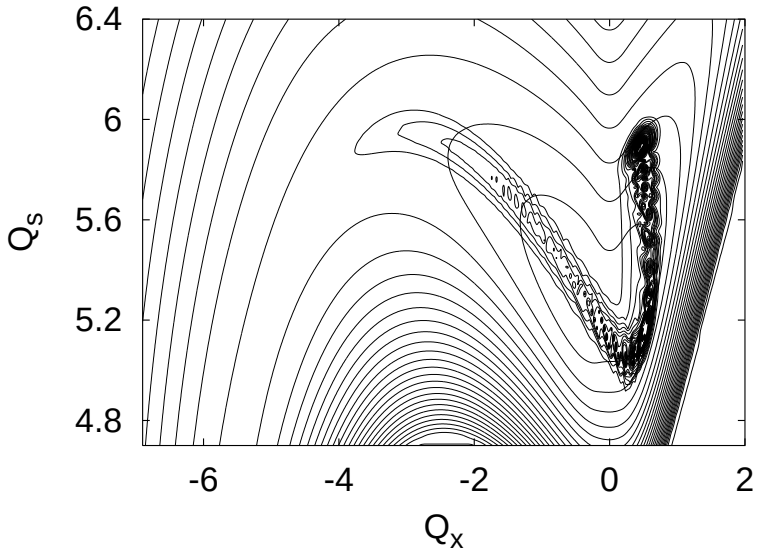

(a)

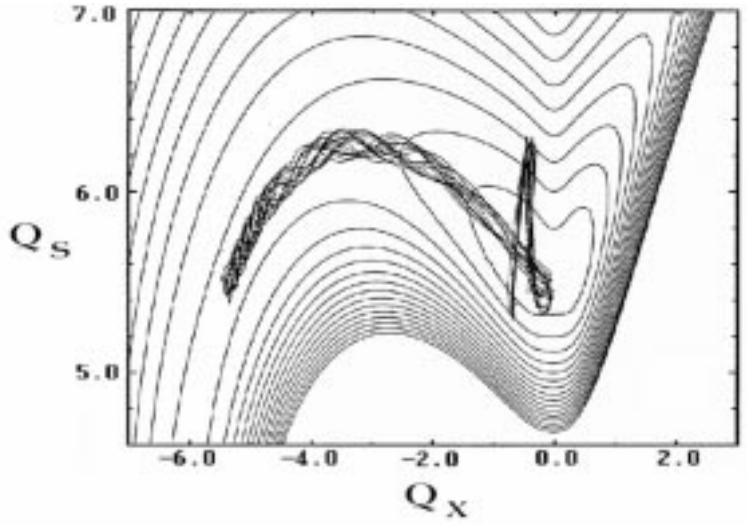

(b)

Figure 3.9: Comparison between quantum mechanical and semiclassical dynamics of Ag_3. (a) Quantum mechanical wave packet at t=1.2 ps, resulting from the first vibrational excited state of Ag_3^-, with the average energy of 57 K.(b) Classical trajectories of the 1.2 ps duration, corresponding to a canonical ensemble of Ag_3^- with 50 K initial temperature [97]

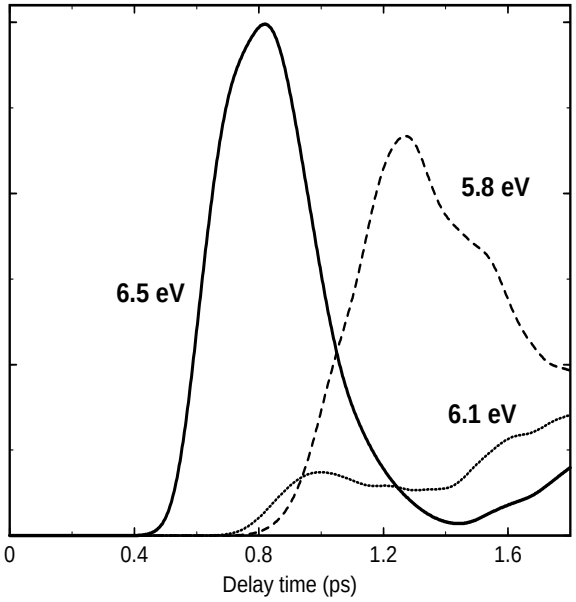

(a)

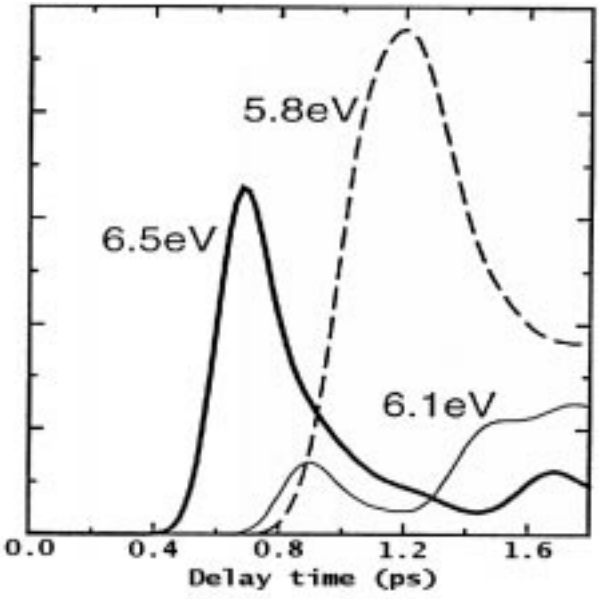

(b)

Figure 3.10: Comparison of theoretical NeNePo-ZEKE spectra of Ag_3 (arbitrary units) obtained from quantum (a) and semiclassical (b) simulations adapted from Ref [97] (see the text for a discussion).

in figures 3.10a and 3.10b respectively. The probe frequencies were chosen to probe the evolving wave packet, or classical phase space density, at three characteristic domains on the potential energy surface during the evolution. The 6.5 eV probe samples the system in the vicinity of the linear geometry, the 5.8 eV pulse covers the region of triangular geometries, and the 6.1 eV value is chosen as an intermediate point.

The calculated semiclassical [97] and quantum NeNePo-ZEKE spectra exhibit common features, and are also in good quantitative agreement. Nevertheless, some differences can be observed. The semiclassical signals are narrower, and shifted to shorter delay times. Also to note is the different relative height of the signals for 5.8 eV and 6.5 eV in the quantum mechanical and semiclassical case. These phenomena can be explained, first, in terms of the different initial ensembles, with higher average kinetic energy in the semiclassical case, and second, by the quantum mechanical spreading of the wave packet, which features prominently in quantum mechanical simulations and, as our working hypothesis, cannot be directly approached in the semiclassical case. Both the semiclassical and quantum mechanical results correspond well to the experimental data of Refs [84, 91].

3.4 Influence of the initial temperature

The simulations of the dynamics of silver trimers using the first vibrational excited state as a starting point, as described in the previous section, already illustrate the characteristic features and timescales of the geometrical relaxation in neutral trimers quite adequately. However, as shown in the semiclassical simulations [97], the temperature of the initial anionic ensemble does influence the dynamics significantly. The rigorous treatment of the temperature effects requires the use of the density matrix formalism, which in the case of Ag_3 is clearly prohibitive.

As an alternative, we use the quantum mechanical superposition principle, and calculate the NeNePo-ZEKE spectra for each of the low-lying vibrational eigenstates independently, and then sum their contributions with the respective Boltzmann

weights as follows:

$$S(t_d, T) = \sum_{v=0}^{4} \mathrm{e}^{-\frac{E_v}{kT}} S_v(t_d, T), \tag{3.7}$$

where the contribution of the v-th eigenstate is defined as an absolute value of the overlap of the time-dependent wave packet $|\psi_v(t)\rangle$ with a certain (unknown) state $|\psi^{(+)}\rangle$, which allows efficient detection of the Ag_3 cations:

$$S_v(t_d, T) = |\langle\psi^{(+)}|\psi_v(t)\rangle|^2. \tag{3.8}$$

Using a semiclassical approximation [97], we obtain the following expression for the signals of individual eigenstates:

$$S_v(t_d, T) = \sum_{G} \mathrm{e}^{-\frac{\tau_{\mathrm{pr}}^2}{\hbar^2}\{E_{\mathrm{pr}} - V_{\mathrm{NC}}(Q_x, Q_y, Q_s)\}^2} |\Psi_{\mathrm{N}}^{v}(Q_x, Q_y, Q_s; t_d)|^2. \tag{3.9}$$

Here T is the initial vibrational temperature of the anionic ensemble, v is the vibrational quantum number, E_v is the excess energy of the quantum state v, Ψ_{N}^{v} is the time-dependent wave function evolving from the v-th eigenfunction of the anion.

Let us prove the validity of the expression (3.7) for the NeNePo-ZEKE signals. Initially, the quantum state of the anionic ensemble is described by the density matrix

$$\hat{\rho}(0, T) = \sum_{v} |\psi_v(0)\rangle \mathrm{e}^{-\frac{E_v}{kT}} \langle\psi_v(0)|, \tag{3.10}$$

where $\psi_v(t) = \Psi_{\mathrm{N}}^{v}(t)$. The evolution of this density matrix is described by the Liouville-von Neumann equation in the absence of dissipation:

$$\mathrm{i}\dot{\hat{\rho}}(t) = [\hat{\mathrm{H}}(\mathrm{t}), \hat{\rho(t)}]. \tag{3.11}$$

At any given moment of time the "propagated" density matrix can be written as follows:

$$\hat{\rho}(t, T, \text{laser} \quad \text{parameters}) = \sum_{v} |\psi_v(t)\rangle \mathrm{e}^{-\frac{E_v}{kT}} \langle\psi_v(t)|. \tag{3.12}$$

Table 3.2: Energies of the low-lying vibrational eigenstates of Ag_3^-

v	(v_s, v_b, v_{as})	Energy , cm^{-1}	Energy , kT	Boltzmann weight (T=50 K)
0	(0,0,0)	0	0	1.000
1	(0,1,0)	31	57	0.320
2	(0,2,0)	62	115	0.100
3	(0,3,0)	92	173	0.034
4	(1,0,0)	110	205	0.016

Note that in order for Ag_3 cations to be detected, the system has to find itself in a certain quantum state $\psi^{(+)}$. Then, the cation yield, or the sought NeNePo-ZEKE signal, can be calculated the following way:

$$\begin{aligned} S(t,T) =& \langle\psi^{(+)}|\hat{\rho}(t)|\psi^{(+)}\rangle = \sum \langle\psi^{(+)}|\psi_v(t)\rangle \mathrm{e}^{-\frac{E_v}{kT}} \langle\psi_v(t)|\psi^{(+)}\rangle \\ &= \sum |\langle\psi^{(+)}|\psi_v(t)\rangle|^2 \mathrm{e}^{-\frac{E_v}{kT}} = \sum S_v(t,T)\mathrm{e}^{-\frac{E_v}{kT}}, \end{aligned} \tag{3.13}$$

Q.E.D.

The energies of the first five low lying eigenstates of the anions are shown in Table 3.2. First column of the table contains the vibrational quantum number, the second - the assignment of the number of quanta in the normal modes of linear Ag_3, third and fourth - the energies of the eigenstates in wavenumbers and units of kT, respectively, and the last one - the Boltzmann weighing factor calculated for the temperature of the anionic ensemble of 50 K. As we can see from the magnitude of the weighing factors in Table 3.2, the five lowest eigenstates should represent the initial ensemble quite adequately. The temperature of 50 K has been chosen to allow the comparison with the semiclassical theoretical results of Ref. [97].

In order to obtain the combined NeNePo-ZEKE signal for a given temperature, the first five lowest-lying eigenstates have to be propagated separately. Then, these "pure" contributions are summed according to the equation (3.7) to yield the desired

signal. The results of these calculations are presented in Figure 3.11, where the top graph shows the combined signal corresponding to the temperature of 50 K, and below the contributions from different eigenstates are presented.

One can see, as expected, that the NeNePo-ZEKE spectra for the thermal ensemble at T=50 K are, firstly, broader than in the $v = 1$ case, and secondly, they are shifted to shorter times, indicating the greater excess of energy. The signals corresponding to different values of the vibrational quantum number v highlight the latter trend. The characteristic maxima of the signals appear at earlier times, when the v is increased. An interesting exception is the $v = 4$ case, where the signal for $v = 0$ is almost duplicated. Also to note are the complex relationships between the quantum number and the character of the signals.

To explain these trends one has to consider the dynamics of the respective wave packets, presented in Figures 3.12-3.16 (For the values of contours of potential and wave function, see the caption to Figure 3.6). The ground state (Figure 3.12) exhibits the most pronounced spreading behaviour, which manifests itself in broad signals of relatively low peak intensity. The first vibrational excited state, $v = 1$ (Figure 3.13), the dynamics of which was investigated in detail above, has one node in the wave function. This node is located at the saddlepoint of the PES of Ag_3^0, which is therefore avoided, resulting in faster dynamics, during which the wave packet stays more compact. Hence, the NeNePo signals for the $v = 1$ case are narrower, and have higher peak intensities. Also, the maxima of the signals occur at the delay times approximately 0.2 ps smaller than in the $v = 0$ case, indicating greater excess of kinetic energy. The signals for the next vibrational eigenstate, $v = 2$, (Figure 3.14), confirm these trends. The initial wave packet has two nodes, resulting in even lesser degree of spreading, and faster dynamics. The signal for 6.1 eV probe energy exhibits an interesting feature, namely the deep minimum at delay time $\approx$ 1.1 ps, followed by further increase. The emerging minimum can also be seen at the 6.5 eV curve, although there it is quite weak. The origin of this becomes clearer after consideration of the evolution of the corresponding wave packet (Figures 3.14b and 3.14c). The nodal structure of the wave function is preserved at the stages of propagation preceding the intracluster collision, and the minimum

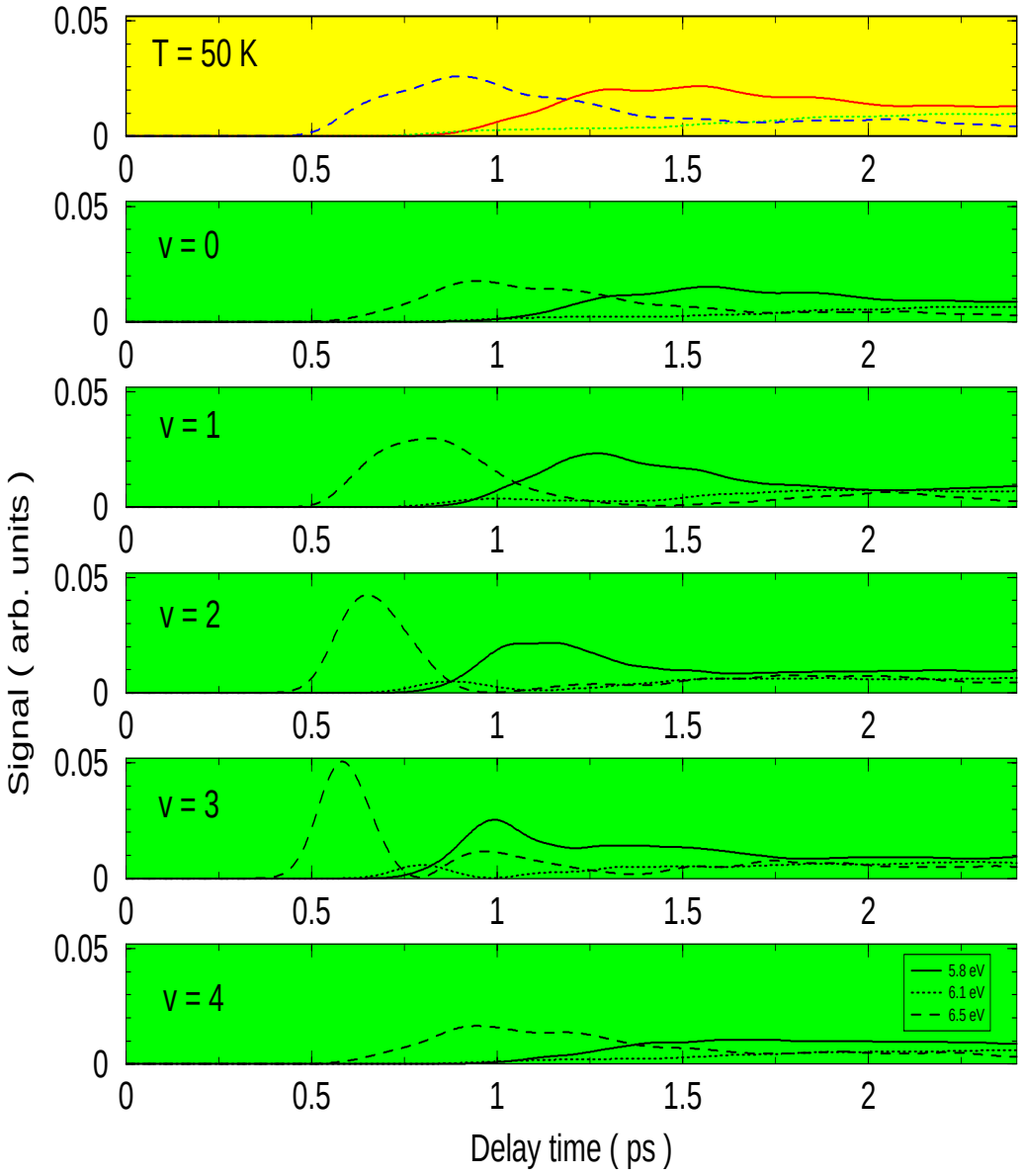

Figure 3.11: NeNePo-ZEKE signal at T=50 K, together with the contributions from low- lying thermally populated vibrational eigenstates of Ag_3^-

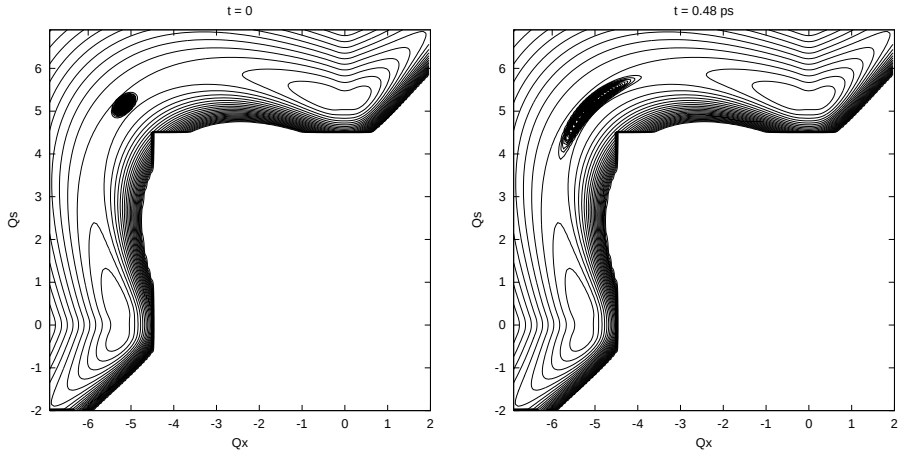

(a)

(b)

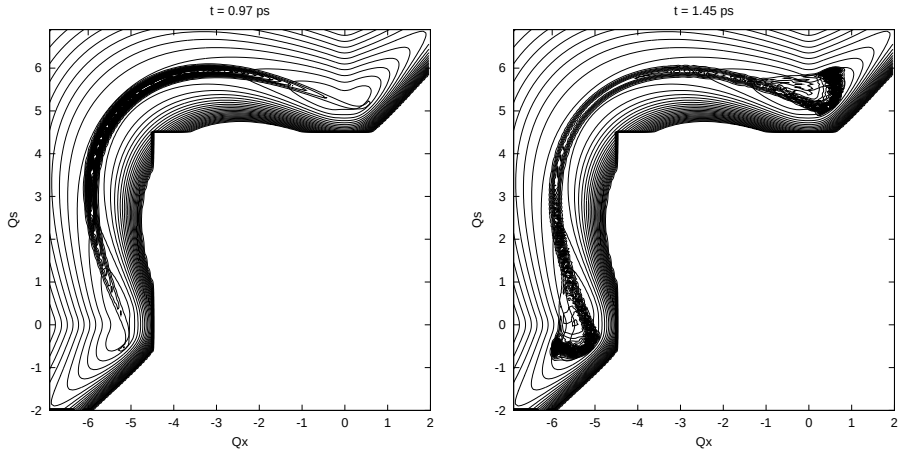

(c)

(d)

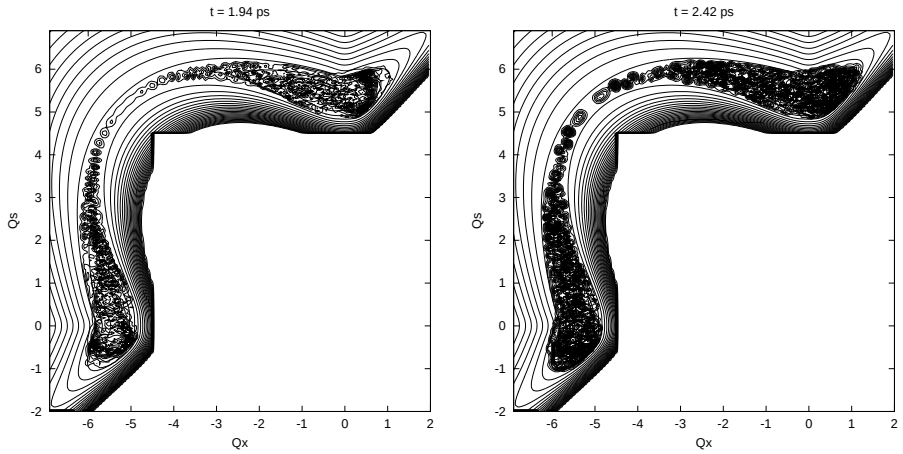

(e)

(f)

Figure 3.12: Evolution of the $v = 0$ eigenstate. For the contour values see figure 3.6.

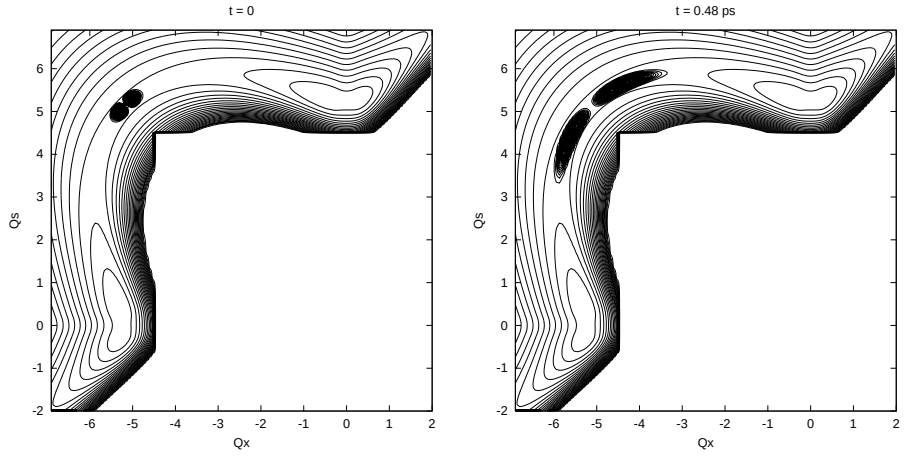

(a)

(b)

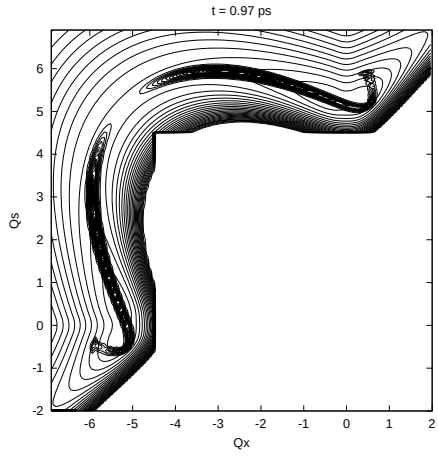

(c)

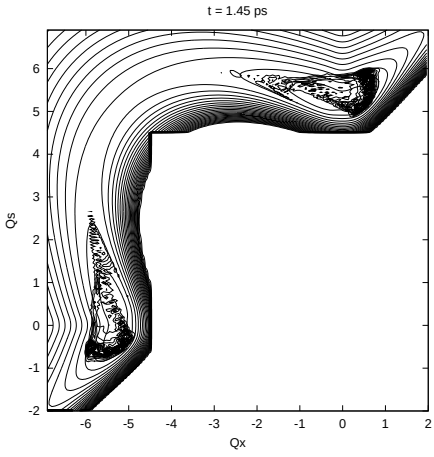

(d)

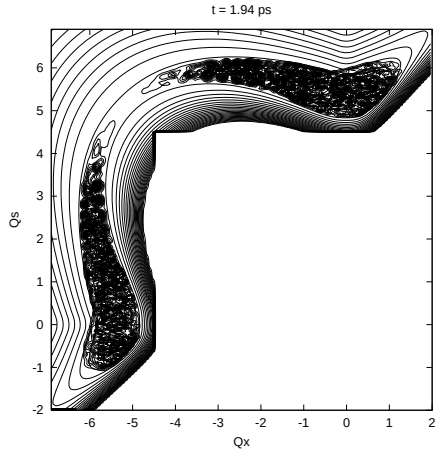

(e)

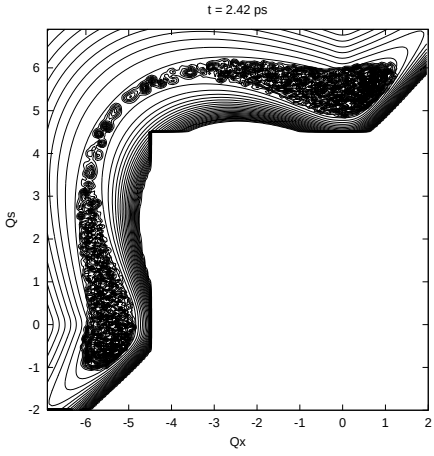

(f)

Figure 3.13: Evolution of the $v = 1$ eigenstate. For the contour values see figure 3.6.

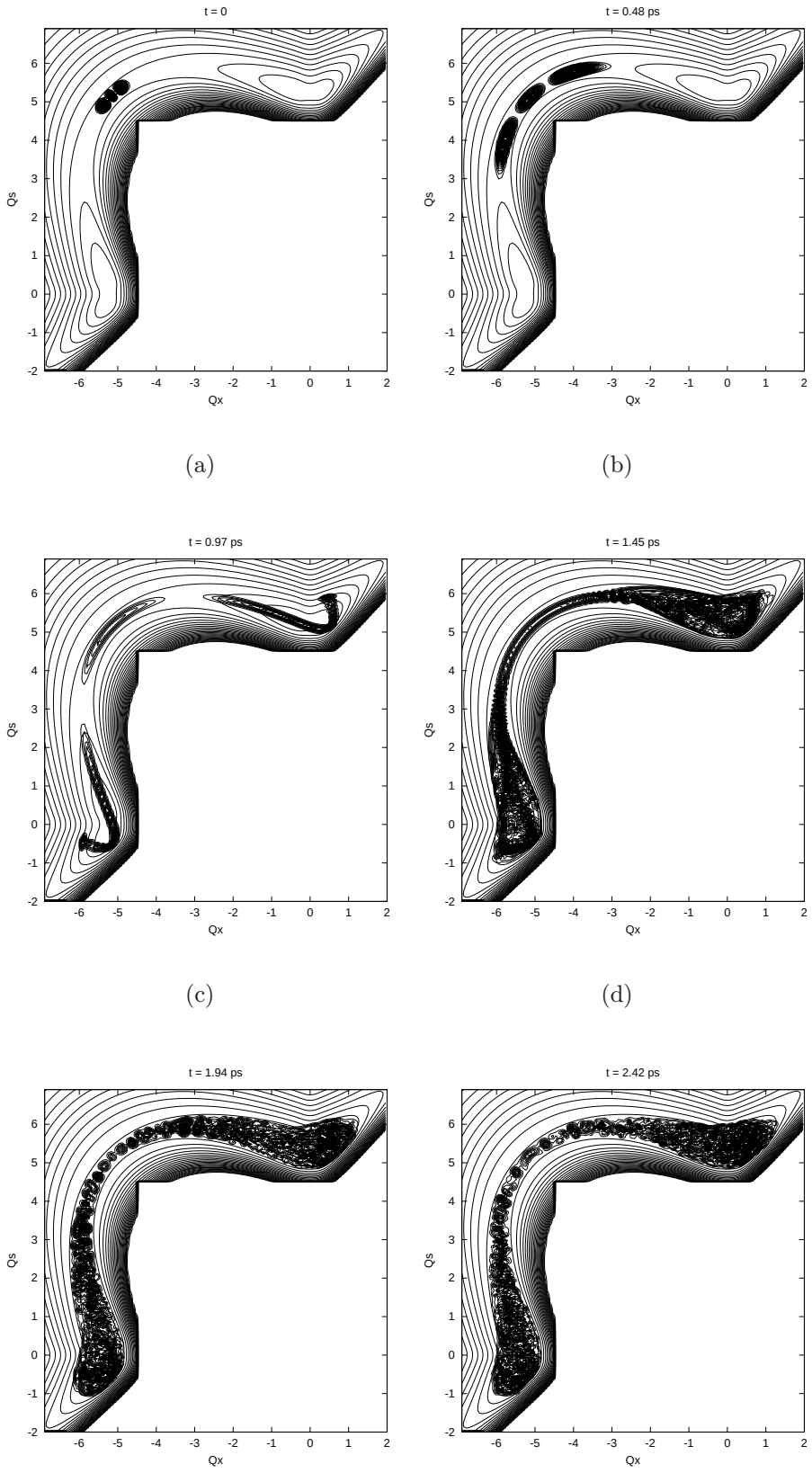

(a) (b) (c) (d) (e) (f)

Figure 3.14: Evolution of the $v = 2$ eigenstate. For the contour values see figure 3.6.

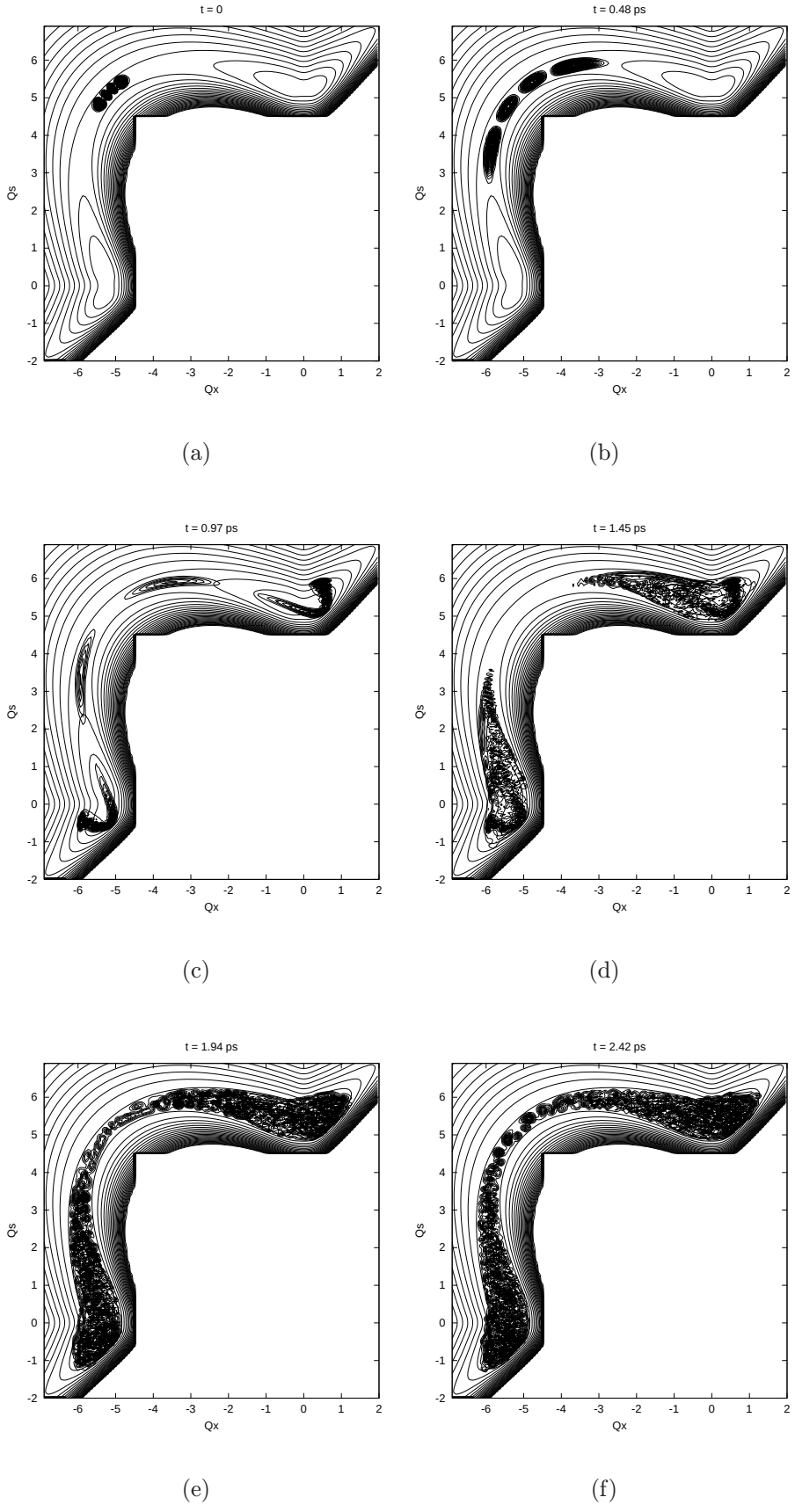

Figure 3.15: Evolution of the $v = 3$ eigenstate. For the contour values see figure 3.6.

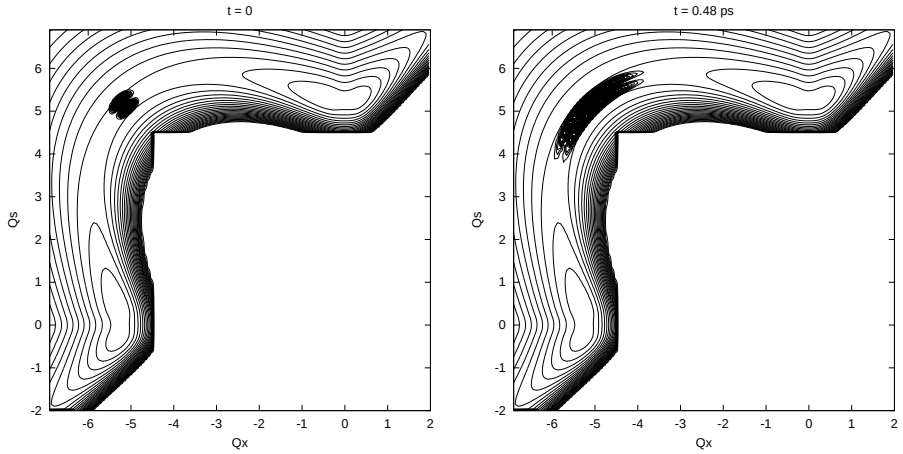

(a)

(b)

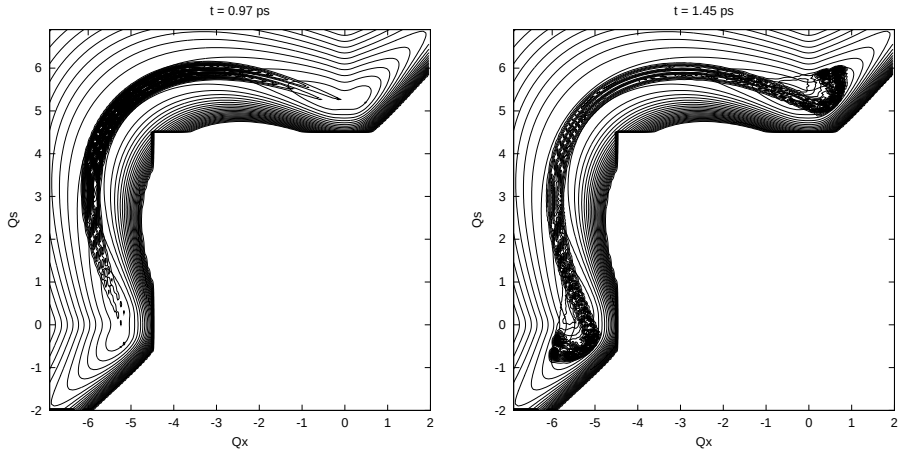

(c)

(d)

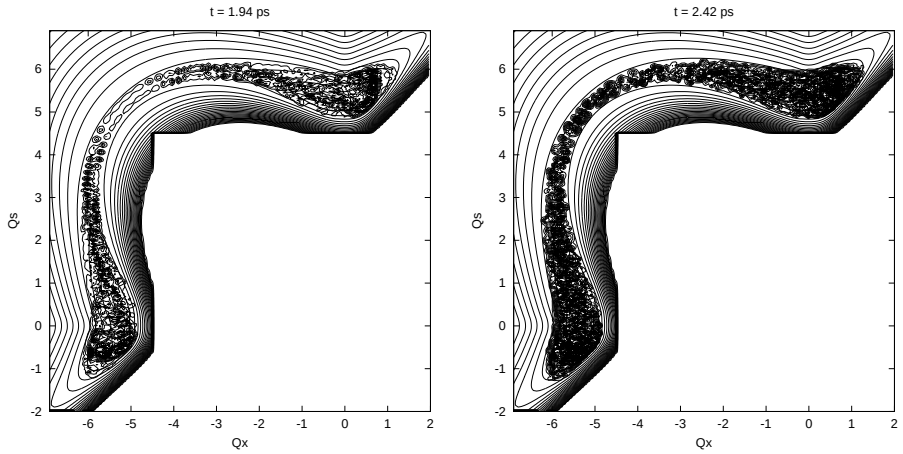

(e)

(f)

Figure 3.16: Evolution of the $v = 4$ eigenstate. For the contour values see figure 3.6.

in the signal emerges at the times, when the node passes the region of the Franck-Condon transition. The signals for the $v = 3$ initial state (Figure 3.15) have two minima, confirming this interpretation.

By considering the snapshots of the wave packet evolution, we are also able to explain the seemingly abnormal behavior of the signals for $v = 4$ initial state (Figure 3.16). The wave function for this state has one node in the direction perpendicular to the reaction path, corresponding to the excitation of the symmetric stretch of Ag_3^-. The two lobes propagate independently until the IVR sets in, and their propagation is almost identical to that of the ground vibrational state $v = 0$. Since in

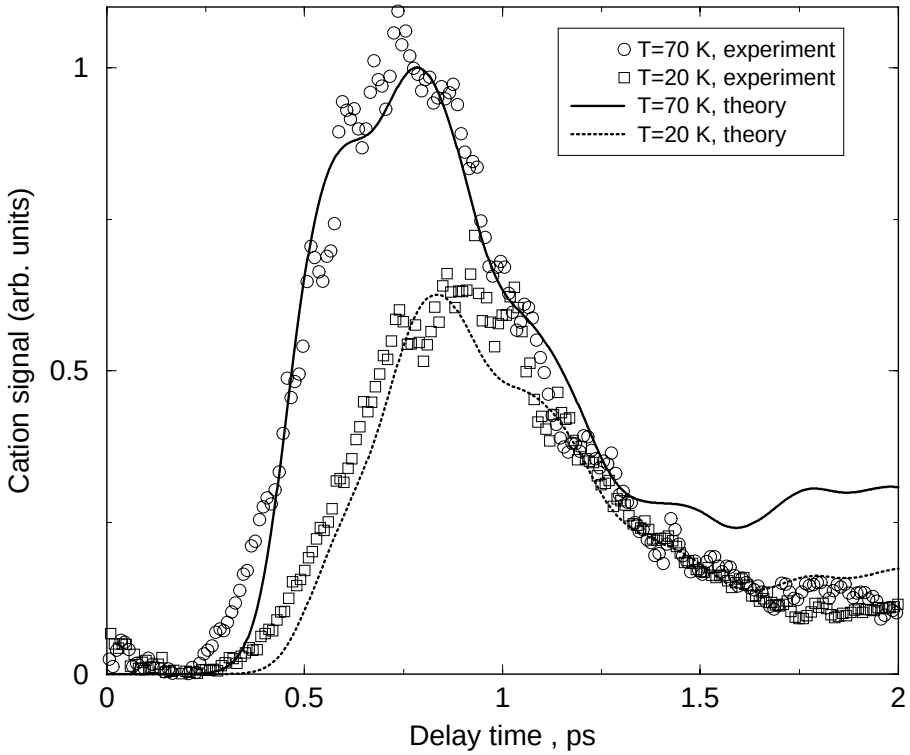

Figure 3.17: The experimental NeNePo signals for two selected temperatures of the anionic ensemble, in comparison with the ones calculated within a 3-D quantum mechanical model for the two-photon probe energy of 6.5 eV.

Franck-Condon approximation the electronic transition occurs in the vicinity of the equipotential contours of the difference potential (see equation 3.6) corresponding to

the excitation energy, and these contours are perpendicular to the reaction path, we cannot distinguish between the contributions of different lobes of the wave function in this case. Hence, the NeNePo signals for $v = 4$ are almost a duplicate of those for the ground $v = 0$ state. There are some marginal differences in the signals after the onset of IVR, owing to the greater excess of kinetic energy in the $v = 4$ case.

It is appropriate now to compare the theoretical results with the latest experimental data obtained by Hess et al. in the group of Wöste [94, 109]. Employing an efficient cooling technique for the anion beam, they have obtained the NeNePo signals for low temperatures of the anionic ensemble. In these experiments, as in recent work by Leisner et al. [92], resonant two photon ionization was employed, which results in very low kinetic energies of ejected electrons, almost approaching the ZEKE case. This enables the direct comparison with the experiment. The results of this comparison are presented in Figure 3.17.

The signals have been normalized in such a way that the maxima of the peaks for the temperature of 70 K have equal height. Otherwise, the magnitudes of the experimental signals with respect to each other were not corrected. As one can see, the 3-D quantum mechanical approach to the dynamics of the silver trimers allows to reproduce the experimentally observed signals with high degree of accuracy. The difference between the experimental and simulated signal for the anion temperature of 70 K after the delay times of 1.5 ps can be attributed to the poorer quality of reconstruction of the thermal ensemble, when only five states are utilized (the Boltzmann weight of the $v = 4$ state for T=70 K is 5%).

It should be noted, that based on the complementary experimental evidence, the experimental signals correspond to both quantum mechanical and semiclassical theoretical results only when the constant factor of 0.4 eV is subtracted from the potential energy of Ag_3^+, thus lowering the IP [94,109]. This may indicate that the *ab initio* quantum chemistry calculations, whilst providing very good relative accuracy of a PES (the good agreement of both semiclassical and quantum mechanical results with the experiment justifies this), give the absolute values of the energies with lower accuracy. A similar effect had to be taken into account in the quantum mechanical simulation of Na_3 [70].

Another important aspect, which should be taken into account when considering the comparison of the both semiclassical and quantum mechanical results with the experiment, is the fact that the models utilized in both theoretical approaches do not accomodate the effects arising in the process of a *resonant* two-photon transition, which involves an electronically excited states as an intermediate one. The PES for this intermediate state is not known, and it may be that the agreement between the theory and the experiment is fortuitous, due to the fact that PES the unknown state Ag_3^* is "parallel" to that of Ag_3^0, that is, not having repulsive sections in the interaction regions of interest. Another (unknown) source of uncertainty is the previously discussed Condon approximation. However, the very good level of agreement between the theoretical and experimental findings suggests that the assumptions made when formulating the physical model have been justified.